Available online at www.sciencedirect.com
ScienceDirect
Journal of the European Ceramic Society 31 (2011) 3109–3118
www.elsevier.com/locate/jeurceramsoc

Influences of the processes on the microstructures and properties of the plasma sprayed IT-SOFC anode

Yung-Chin Yang *, Yu-Chun Chen

Institute of Materials Science and Engineering, National Taipei University of Technology, Taipei 106, Taiwan

Available online 25 May 2011

Abstract

By using the atmospheric plasma spraying (APS) technique for SOFC fabrication, we can avoid the thermal failure between the components of SOFC which made from the traditional sintering method at high temperature. The advantage of porous metal supported SOFC produced by the APS process is that the process is simple and low cost. The purpose of this study was to manufacture a porous Ni/CeO_2 anode of intermediate temperature SOFC. By introducing the pore former into the feedstocks, the porous structure of the Ni/CeO_2 anode was obtained by plasma spraying method. In this study, the feedstock of the $NiO/CeO_2/Na_2CO_3$ powder made by the spray granulation is spherical; the powder structure is compact and a hollow hole inside the powder, hence more porosity (29.1%) of the as-sprayed coating was found and the pore distribution is more uniform. The remainder oxygen vacancies are existed in the reduced anode coating. Use of undoped ceria as an anode material appears to be feasible. The $NiO/CeO_2/Na_2CO_3$ powder formed the higher bonding strength coating with 33.6 MPa. The electron conductivity was obtained with around 200 S/cm in 700 °C. The other properties of the anode were discussed in the paper.

Keywords: Plasma spray; Anode; SOFC

1. Introduction

Solid oxide fuel cells (SOFCs), which use solid oxides as electrolyte, are electrochemical devices that transform the chemical energy of fuel (hydrogen natural gas, etc.) directly to electrical energy. SOFC possesses some unique advantages over the traditional power generation technologies, including inherently high efficiency, low greenhouse emissions and fuel flexibility. As highly efficient and pollution-free energy sources SOFCs have been intensively studied during the past decade.[1]

Conventional solid oxide fuel cells (SOFCs) based on yttria stabilized zirconia (YSZ) are normally operated at very high temperatures, above 800 °C. High-temperature operation that induces considerable reactions at electrode/electrolyte and electrode/interconnect interfaces, resulting in deteriorated cell performance and lifetime. To overcome these problems, most recent research and development activities have focused on the development of intermediate-temperature solid oxide fuel cells (IT-SOFCs) that can be operated at a temperature range of 500–700 °C.[2–5] The research and development of SOFCs operated at 500–700 °C is very important because it can lead to the use of low-cost metallic alloys in SOFCs with a fast start-up.

Several approaches of fabricating SOFC components are existed. They include chemical vapor deposition (CVD), electrochemical vapor deposition (EVD), sol–gel method, tape-casting, screen-printing, physical vapor deposition (PVD) and plasma spraying.[6–15] Among these approaches, atmospheric plasma spraying (APS) is a fast process, no or only slight post processing of the product is necessary. It is known that the conventional thin film techniques, such as tape casting, screen printing and dip molding, have to go through a high temperature sintering process. For large area cells, this step will inevitably introduce a lot of defects, such as warp, crackle and pore. Meanwhile, high temperature sintering processes can also induce reactions

* Corresponding author.
E-mail address: ycyang@ntut.edu.tw (Y.-C. Yang).

0955-2219/$ – see front matter © 2011 Elsevier Ltd. All rights reserved.
doi:10.1016/j.jeurceramsoc.2011.05.001

between function layers, but, the plasma spraying process is a fast sintering process, interaction between electrode interface could be reduced.[16,17] The main advantage of porous metallic supported thin-coating cell fabricated by APS is to allow enlarging the cell area without sintering defects and improve its mechanical properties.[18] In addition to high material deposition rates, plasma spraying processes can easily control the component composition and microstructure through variation of spray parameters, hence, plasma spraying process has thus appeared as a promising candidate for inexpensive and fast cell production, and attracted much attention.[17,19]

As stated, the porous structure in a plasma sprayed anode for SOFC might be very important for the efficiency of the cell system and success in application, but, academic studies on this subject are scarce. In the work of Zheng et al.,[20] Ni/8YSZ anode coating were deposited onto a porous Ni-plate substrate by atmospheric plasma spraying. By proper selection of the spray parameters to decrease the particles velocity and temperature, the sprayed NiO/8YSZ coating after reducing with hydrogen shows a good electrocatalytic activity for H_2 oxidation. Hwang et al. used the agglomerated nanostructured NiO/YSZ powders to produce nanostructured NiO/YSZ coatings by plasma spraying.[21] After reduction in 7% hydrogen, a novel SOFC anode with nano pores and nano pore channels were produced. These nanostructured features can provide more triple phase boundaries for hydrogen oxidation reactions and that are expected to have a lower polarization loss for SOFC anode applications. Ma et al. mentioned that a porous Ni/LDC anode layer has been produced in the solution precursor plasma spray (SPPS) process.[22] The SPPS-deposited anode coating is highly porous with porosity 40–45%. Unlike the case of disk-like pores in conventional plasma spraying, the SPPS will produce near-sphere shaped pores. However, the over porosity might damaged the anode structure and lower the durability of cell system, especially for the anode support SOFC. In the past work, it was shown that Young's modulus of NiO-YSZ decreases almost by half with increase in porosity from 0 to 23 vol%.[23]

Among the most used electrolyte materials, ceria, in particular, represents a considerable challenge because of its insulating properties, remarkable chemical stability and small lattice mismatch with Nickel.[5] At present, a cermet consisting of Ni-metal and doped ceria is widely used as an anode material in intermediate temperature SOFCs. Coating prepared through plasma spray process from high temperature (over powder melting point) to rapid cooling contains plenty of amorphous phases and displayed the low crystallinity. For electrolyte material, the plasma sprayed undoped ceria coating represents partial amorphous structure, it could be considered as the conduction path of oxygen ion. Due to the low cost of undoped ceria as compared with SDC or GDC, the plasma sprayed undoped ceria with ionic conductivity might be a low cost electrolyte for industrial application. Therefore, in the present study, the undoped ceria was employed. The porous electrode coating of Ni/CeO_2 on the stainless steel was made by the plasma spraying. We introduced the Na_2CO_3 powder as the pore former into the NiO/CeO_2 composite powder, the composite $NiO/CeO_2/Na_2CO_3$ powder from the spray granulation was employed for the plasma spraying. The microstructures, porosity, phase composition and crystallinity of the anodes made from various spraying parameters were compared.

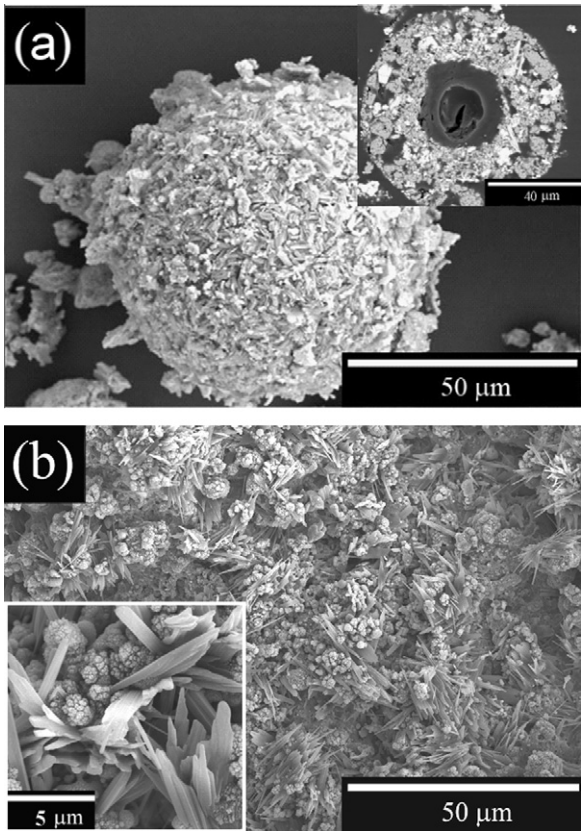

Fig. 1. (a) Morphology and cross-sectional view of the $NiO/CeO_2/Na_2CO_3$ composite powder, (b) morphology of the as-sprayed N1 coating and the magnified needle-like crystal.

2. Materials and methods

2.1. Specimens preparation

In this study, the commercial NiO with particle size of 0.2–0.5 μm and the CeO_2 with particle size of 0.07–0.1 μm were employed as the raw materials. Composite powder for plasma spraying process was fabricated by spray granular method (spray dry) after ball milling. The composition of the composite feedstock is NiO, CeO_2 and the Na_2CO_3 as the pore former ($NiO:CeO_2:Na_2CO_3 = 6:4:1$ wt%). Fig. 1(a) shows the morphology of the granulated feedstock with around 30–70 μm in diameters with a good flowability, which is suitable for the plasma spraying process. The inset is the cross sectional microstructure of the powder. The typical structure with a shrinked hole was found after the drying and granulating process. In the porous shell part, the gray NiO and white CeO_2 particle were mixed well with pore former.

Among all fabrication techniques, the atmospheric plasma spray (APS) procedure seems to be the most cost-effective method. One more important advantage is that APS is effective for any shape of substrate, so that the coating could be

Table 1
Plasma spraying parameters of the $NiO/CeO_2/Na_2CO_3$ coating.

Spraying parameters	$NiO/CeO_2/Na_2CO_3$	
	N1 coating	N2 coating
Power (kW)	50	25
Torch current (A)	660	660
Primary gas (Ar) (l/min)	50	50
Secondary gas (H_2) (l/min)	14	0
Stand-off distance (cm)	7.5	7.5
Feedstock carrier gas (l/min)	2.5	2.5
Powder feed rate (rpm)	20	20
Surface speed, Vs (rpm)	150	150
Transverse speed, Vt (mm/sec)	5	5

easily coated on the tubular substrate. Discs of 304 stainless steel, measuring 3 mm (t) × 25.4 mm (ϕ), were selected as substrates. Prior to spraying, all the substrates were cleaned in acetone ultrasonically and then grit blasted with Al_2O_3 sand to roughen the surface (Ra = 3.5 μm). In plasma spraying process, the feedstock powder was carried by high purity argon gas to the plasma torch of the plasma spraying system (Sulzer Metco), the feedstock powder were vertically injected into the plasma jet center and then highly deposited onto substrate. The spraying parameters and specimen conditions are shown in Table 1, two spraying power 50 kW and 25 kW were employed and two kinds of anode coating were prepared (N1 and N2). The as-sprayed $NiO/CeO_2/Na_2CO_3$ anode was soaked in DI water to remove the pore former (Na_2CO_3). Finally, the soaked anode coating was processed with reduction treatment at 800 °C for 2 h in the atmosphere of 5% hydrogen, and then the Ni/CeO_2 anode was obtained.

2.2. Characterization of plasma sprayed anode

The melting characteristics of the feedstocks were assessed from the surface morphology of the sprayed anode coatings via SEM. The porosity of the coatings were examined cross sectionally by BEI (backscattering electron image) of SEM, and then quantitatively determined by an image analyzer (Image-Pro Plus 5.0). The phase constituents of the anode coating and the prepared feedstocks were identified by X-ray diffractometry. Moreover, the index of crystallinity (IOC, %) of the coating was evaluated from the ratio of the main peak intensities of the anode coating (I_c) and the raw powder (I_p) by the relation of IOC (%) = $(I_c/I_p) \times 100\%$.[24,25] This method suggests that the IOC of the raw powder is 100%. To ensure that the data obtain correctly, all the measurements must be carried out under the same conditions, such as sample weight, X-ray diffractometer's conditions and parameters of measurement.

The Raman mode of cerium and the oxygen vacancy in the as-sprayed and reduced anode coating were obtained from the Raman shift profile. Raman spectra were taken in the backscattering configuration and analyzed using Omicron Laser Controller software. We used the 532 nm line of laser as an excitation source. The conductivity of the reduced Ni/CeO_2 anode was measured in the atmosphere of 5% hydrogen from room temperature to 800 °C by the DC four-terminal method using Agilent Technologies 34970A and 6645A data acquisition/switch units with silver as the metallic electrode and wire.

The bonding strength of the anode coating was tested using a standard adhesion test (ASTM C-633)[26] that was especially designed for plasma-sprayed coatings. The test bar was a cylindrical rod of 304 stainless steel, measuring 2.54 cm in diameter and 5.5 cm in length. Anode coating with a thickness of around 150 μm were plasma sprayed on the substrate fixtures. The facings of the loading fixtures were grit-blasted and attached to the surface of the HACs using special adhesive glue (METCO EP-15) with an adhesive strength of about 60 MPa. The assembly was held perpendicularly and placed in an oven at 180 °C for 2 h. After the bonding glue was cured and hardened, the assembly was loaded in the Instron machine for the measurement of the tensile bonding strength.

2.3. Porous metallic substrate

The powders for the development of metallic substrates were 304 stainless steel and nickel powder, 9 wt% PVA was added as the binder and the pore former. Metallic powders with particle sizes between 10 and 30 μm have been used for the press-less sintering process with which the substrates were produced. The sintering was progressed in the vacuum furnace with 10^{-6} torr. The heating program was holding at 600 °C an hour for debinding and sintering. Then, the metallic powders were sintered at 1000 °C with 1 h, 2 h and 3 h holding time in respectively. The porosity, gas permeability and strength of metallic substrate were evaluated under various sintering time. After then, the NiO/CeO_2 anode coating was plasma sprayed onto the porous metal substrate using the N1 spraying parameters in Table 1.

3. Results and discussion

3.1. Characteristics of N1 anode coating

Fig. 1(b) shows surface morphology of the as-sprayed N1 anode coating. The coated surface reveals high roughness and porosity. From the figure evidently observed are a number of needle-like crystals, known as sodium compounds by EDS analysis. Whether they are sodium oxides or sodium carbonates is yet to be clarified. Compared with what observed in Fig. 1(a), the needle-like crystals were not found in the original feedstock powder, suggesting that they should grow during the melting process. The needle-like crystals could be dissolved after soaked the as-sprayed N1 coating in the water, leaving holes in the coating surface, as shown in Fig. 2. In Fig. 2(a), the observation is apparently porous coating surface with large roughness. The microstructure reveals holes that resulted from dissolution of the needle-like crystals by water, with hole-size of about 1–2 μm or smaller. With the structure that the holes are channeled up-and-down with one another, in SOFC these connected channels will make ventilation for fuel gases. Fig. 2(b) shows cross section of the coating layer under BEI mode. Thickness of the coating layer is about 50–80 μm. Size of the holes distributed in the coating is about 0.5–5 μm. In the structural profile of coating, the light

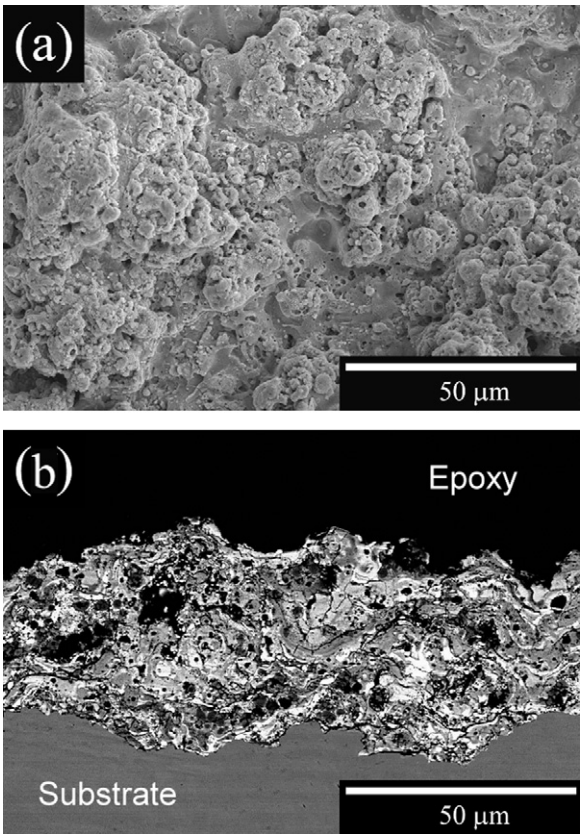

Fig. 2. (a) Morphology of the soaked N1 anode coating with porous and rough surface, (b) cross sectional view of the soaked N1 anode coating with porous structure.

color is cerium oxide while the grayish is nickel oxide. These two materials are uniformly distributed in the coating.

The N1 anode coating was processed then with reduction treatment at 800 °C for 2 h in the atmosphere of 5% hydrogen. Fig. 3(a) shows the resultant surface of the coating, due to volume shrinkage when the nickel oxides were reduced to nickel, observed in the inset are holes of sub-microns (as pointed out by the arrow) besides those formed after the spraying process with addition of pore former. In addition, particles of size about 1 μm were observed on the coating surface, as shown in the position marked 1 of the inset. By EDS analysis, the particles were nickel (Fig. 3(b), spectrum 1). In area of the coating with sub-micron holes (Fig. 3(a), in the position marked 2), the material is composed of nickel and CeO_2 (Fig. 3(b), spectrum 2). Fig. 4(a) shows the cross section of the coating with clear stratum and pore structures. Fig. 4(b) shows that the sub-micron holes are distributed throughout the coating. Increase of these tiny holes enhanced amount of the triple phase boundary (TPB) of the anode coating. Furthermore, by the mapping analysis shown in Fig. 4(b), the uniform distribution of nickel and cerium demonstrates that a large number of TPB were formed in the anode coating layer, increasing conductivity of electrons and oxygen ions in the anode and enhancing the rate of electrochemical reaction.

Fig. 5(a) shows the NiO and CeO_2 diffraction peak of the feedstock ($NiO/CeO_2/Na_2CO_3$ composite powder) made from

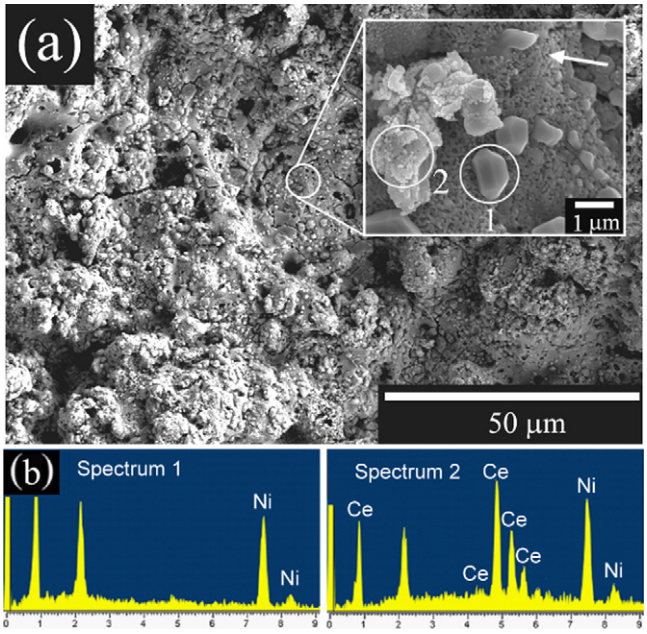

Fig. 3. (a) Morphology of the reduced N1 anode coating, (b) EDS analysis of the particles in the positions marked 1 and 2 in (a).

the spray granulating, while the pore former Na_2CO_3 was not seen in the XRD pattern because of its weak diffraction signal. Fig. 5(b) shows the XRD pattern of as-sprayed N1 anode coating, it can be found that the main composition is NiO and CeO_2, but in the figure observed is a small amount of metallic Ni, formed

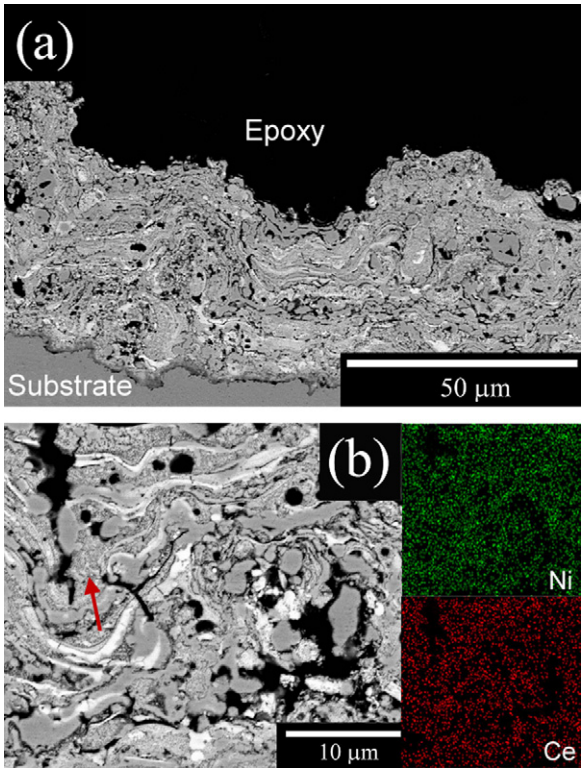

Fig. 4. (a) Cross sectional view of the reduced N1 anode coating, (b) mapping analysis and illustration of the sub-micro channel, pores and cracks in the reduced N1 anode coating.

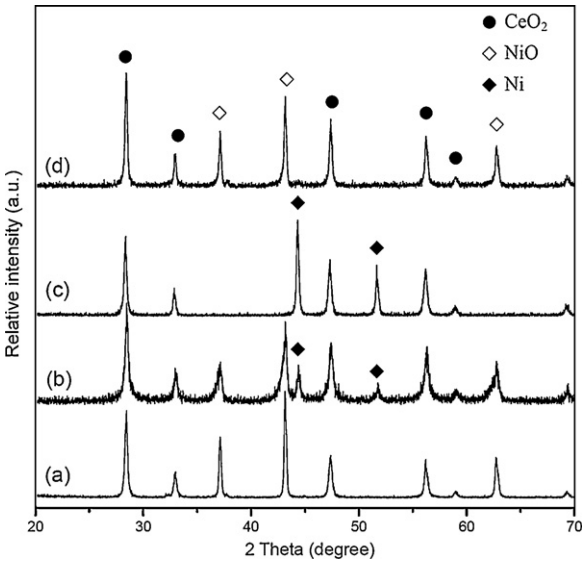

Fig. 5. X-ray diffraction pattern of (a) feedstock powder, (b) N1 as-sprayed coaing, (c) N1 reduced coating, (d) N2 as-sprayed coating.

by reduction of NiO in the spraying process. The XRD pattern of the reduced N1 anode is shown in Fig. 5(c), where the diffraction peak of NiO disappears. Rather, it shows the diffraction peak of metallic Ni. That manifests the coating was a porous anode of Ni/CeO_2 after the hydrogen reduction.

3.2. Characteristics of N2 anode coating

In this study, the gases for plasma spraying are argon and hydrogen (Table 1). The diffraction peak of metallic Ni observed in Fig. 5(b) was presumably that the hydrogen used in the spraying process reduced a small amount of NiO into Ni. As a proof, spraying process did not use H_2 as a secondary gas and spraying power greatly reduced to 25 kW per N2 spraying parameters, as shown in Table 1. The XRD spectrum of N2 anode coating is shown in Fig. 5(d). The diffraction peak of metallic Ni is not observed. It is evident that the use of hydrogen caused reduction of a small amount of Ni in the making of anode coating with the N1 spraying parameters.

Fig. 6(a) shows surface morphology of the N2 coating. Because decrease of spraying power diminished molten state of the coating, the layer was mostly accumulation of semi-molten splats; also, the growth of needle-like crystals was not obvious that resulted from residue of the pore former. The remaining pore former would be dissolved after the N2 coating was soaked in the water, leaving holes on the coating surface, as shown in Fig. 6(b). Compared with the N1 coating, the N2 coating was mostly accumulated by semi-molten splats because of lower spraying power. This phenomenon actually enhanced coating porosity; size of the holes in the N2 coating was about 0.5–3 μm. Fig. 7 shows cross sectional view of the N2 coating with thickness of 50–70 μm after soaked in the water. Because the N2 coating was prepared by low power, the molten state of the powder was lessened but the porosity was enhanced and the pores were uniformly distributed.

In Fig. 8(a) the morphologies of the reduced N2 coating is observed. The volume of nickel oxides shrank during the reduction process, resulting in holes of sub-microns in the coating, besides those formed after the spraying process with addition of the pore former. Fig. 8(b) shows cross sectional view of the coating that contains clear layer and pore structures. It evidently shows that the sub-micron holes distributed throughout the coating. Increase of these tiny holes enhanced the amount of triple phase boundary (TPB) of the anode coating. Compared with the N1 coating, the N2 coating had inferior molten powder and therefore loose coating structure, but the porosity was enhanced and the distribution of pores was more uniform. Moreover, appar-

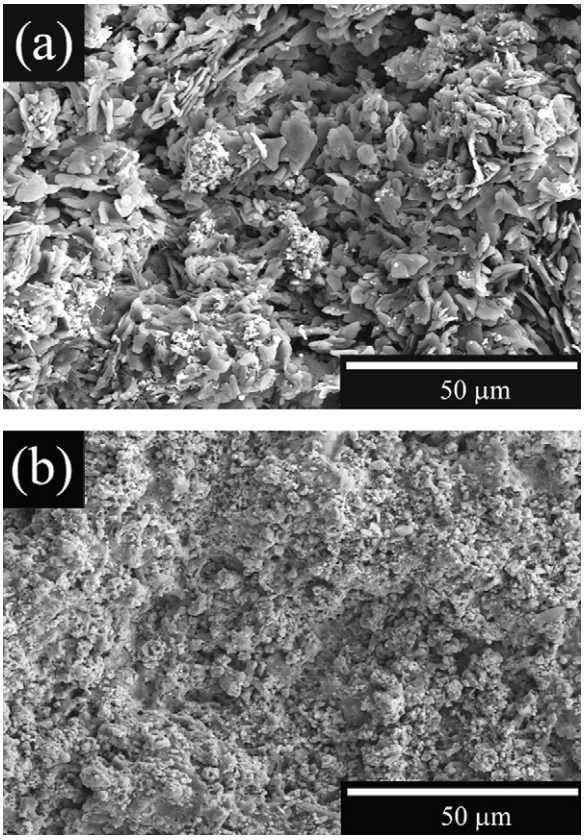

Fig. 6. (a) Morphology of the N2 as-sprayed coating, (b) morphology of the N2 coating after soaking in the water.

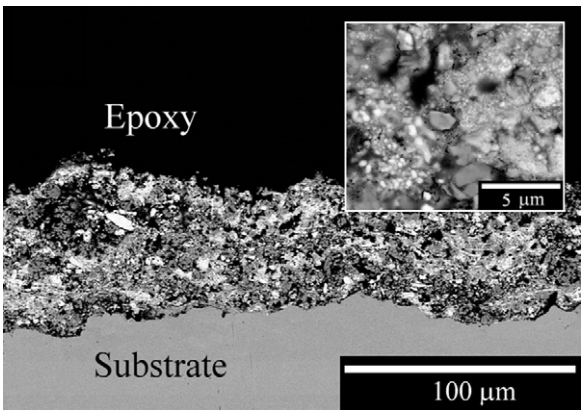

Fig. 7. Cross sectional views of the N2 anode coating soaking in the water.

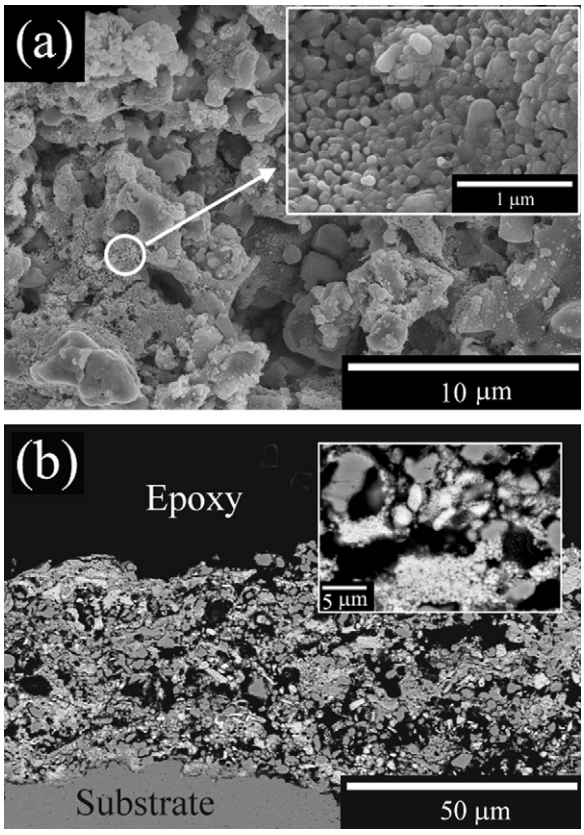

Fig. 8. (a) Morphology and (b) cross sectional views of the reduced N2 anode coating.

ently the number of triple phase boundaries (TPB) was much more than that in the N1 coating.

The porosity of SOFC anode must be greater than 30% for developing better function. Therefore, porosity is an important index in improving anode preparation. Fig. 9 shows the porosity of as-sprayed N1 coating can be up to 29.1% and that of N1 anode is 34.1% after reduction. Furthermore, Fig. 9 also shows the porosity with 32.1% of the as-sprayed N2 coating, and it can be up to 37.2% after reduction. With general plasma sprayed coating, the porosity is only about 20% in the coating. Thus, the addition of pore former to initial composite powder in the granulation process can effectively enhance porosity of the anode coating.

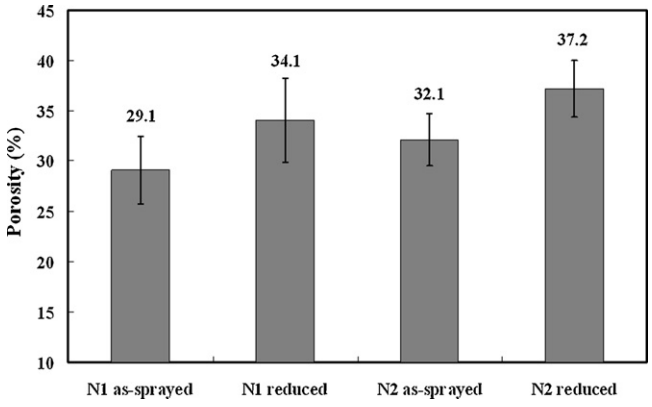

Fig. 9. Porosity of the plasma sprayed anode coatings before and after reduction in H_2 atmosphere.

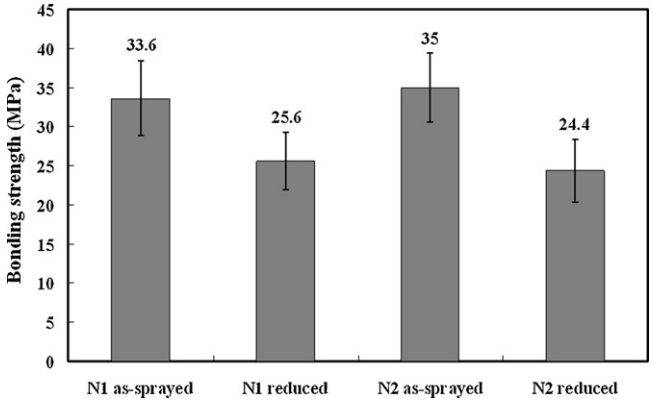

Fig. 10. Bonding strength of the plasma sprayed anode coatings before and after reduction in H_2 atmosphere.

3.3. Bonding strength between anode coating and substrate

Bonding strength between anode coating and substrate is shown in Fig. 10. The bonding strength was 33.6 ± 4.8 MPa for the as-sprayed N1 coating (NiO/CeO_2) prepared by high-power spraying, while that was 25.6 ± 3.7 MPa after reduction, lower than the value before reduction. The difference was mainly due to increase of the porosity in the anode after reduction that affects the bonding strength of the coating. Similar result was obtained with the N2 coating that was prepared by low power spraying, as in Fig. 10, that the bonding strength after reduction (24.4 ± 4.0 MPa) was lower than that before reduction (35.0 ± 4.4 MPa). Moreover, the N1 and N2 coatings were similar in strength of bonding with the substrate. It is worth noting that the porosity of the two as-sprayed coatings was more than 30% and the bonding strength is above 24.4 MPa after coating reduction. Both met the specification of general purpose in requirement of whether porosity or bonding strength of coating.

In this study, thickness of specimens used for bonding strength measurement was above 100 μm, complying with the ASTM-C633 standard. Cross sections of fracture after bonding strength tests and failure modes are shown in Fig. 11. Illustrated in Fig. 11(a) is a schematic diagram of two failure modes: cohesive failure of coatings and adhesive failure of interfaces. The failure mode applied in this study was hybrid breaking. Part of the failure was applied between the anode and the substrate; the other part of the breaking was applied inside the coatings. Viewed from the fracture surface, the failure can be divided into area failure and point failure, as shown in Fig. 11(b). Region A shows point failure that fracture started in the coating or between coating and substrate interface; the section area of each individual facture was very small. Therefore, on the fracture surface, granular protrusions were observed on the loading fixture surface while granular concavities were observed for substrate fixture surface. Region B shows area failure that the section area of single fracture was larger than that of point failure; fracture started in the coating or between coating and substrate interface. From literatures it showed that the lower the bonding strength

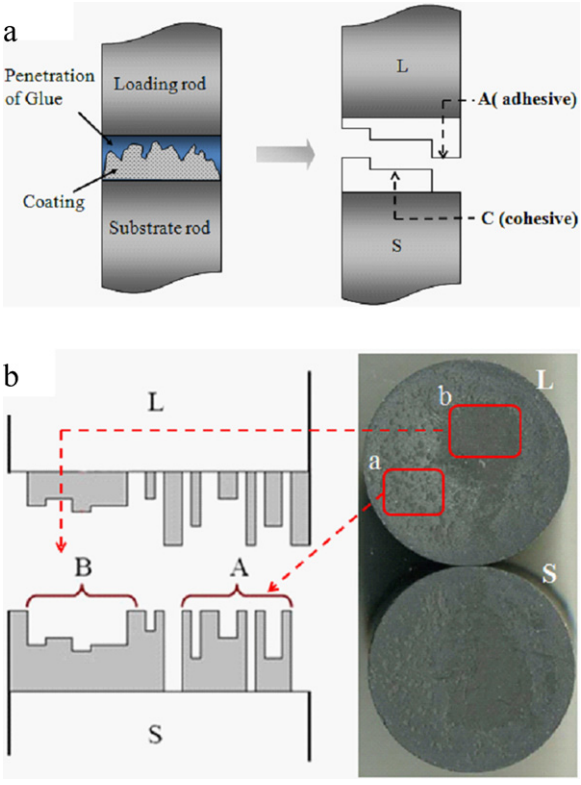

Fig. 11. Illustrations of the failure mode analysis after bonding strength test, (a) illustration of the adhesive and cohesive failure mode in the coating, (b) the failure site observation with the point failure (A) and the area failure (B).

between the coating and the substrate, the more failure tended to be large area failure; on the contrary, the higher the bonding strength, the failures were almost point failure.

3.4. Raman spectra analysis

Raman spectra of plasma sprayed undoped ceria before and after reduction are shown in Fig. 12. These spectra display the intense Raman bands with maximum amplitude at around 454 cm^{-1} and 463 cm^{-1}. The main band of both reduced anode

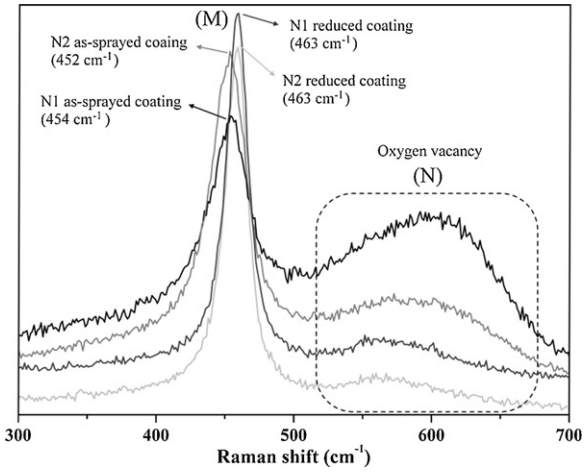

Fig. 12. Raman spectra of the N1 and the N2 coating.

Table 2
Oxygen vacancies in the CeO_2 of anode with various conditions.

	As-sprayed CeO_2		Reduced CeO_2	
	N1 coating	N2 coating	N1 coating	N2 coating
Oxygen vacancy (I_N/I_M)	0.61	0.17	0.06	0.03
Crystallinity, IOC (%)	42%	58%	78%	87%

coating (N1, N2) at 463 cm^{-1} is the only allowed Raman mode, which can be assigned to F_{2g} symmetry as a symmetric breathing mode of the oxygen atoms around the cerium ions in the cubic fluorite.[27–29] Raman mode in as-sprayed N1 and N2 anode are positioned at 454 cm^{-1} and 452 cm^{-1}, respectively. The shift of Raman peak from 463 to 454 cm^{-1} was observed due to the expansion of lattice as the short range order occurred in amorphous ceria, that is, the shifted Raman peak with pronounced asymmetry characteristic for very fine, non-stoichiometric nanocrystals.[30,31] Moreover, the broadening of these two Raman peaks also implies a smaller grain size. The degree of crystallinity and size of crystal grains explained the little difference in the Raman mode of CeO_2 in the coating before and after reduction (454 cm^{-1} vs. 463 cm^{-1}).[32] It was because the crystallinity of coating was low right after plasma spraying as shown in Table 2, and the coating existed more amorphous phases and short range order structures. When the coating was reduced at 800 °C in hydrogen, crystalline phases were recrystallized from the amorphous phases. Thus, crystallinity of the coating was increased and grains also grew. Hence, the symmetry Raman mode of the reduced anode coating at 463 cm^{-1} was observed.

Another broad Raman band near around 560–620 cm^{-1} was attributed to the presence of defects, in our case the defect peak corresponds to disorder in the oxygen sublattice (oxygen vacancies).[28,33] It is also consistent with the results obtained from other characterization studies discussed so far.[30,34,35] Difference in crystallinity and grain size (i.e. the number of grain boundaries) of cerium oxide in the coating also affected the number of oxygen vacancies in undoped cerium oxide. This can be observed in Fig. 12. The ratio of intensity between the Raman band of the oxygen vacancies (N) and CeO_2 (M) served as a relative indicator for the concentration of oxygen vacancies.[36,37] As shown in Table 2, the ratio of oxygen vacancies in as-sprayed N1 and N2 coating are 0.61 and 0.17 in respectively. The difference of the amount of oxygen vacancy is due to the high amorphous content in the N1 coating and that result in the high oxygen vacancy content. After anode reduction, the oxygen vacancies of cerium oxide in the coatings were decreased due to the increasing of crystallinity.

Plasma sprayed coating usually reveals amorphous phase due to the rapid solidification of the melting feedstock. From Table 2, N1 anode made by higher spraying power exhibited lower crystallinity due to the better melting feedstock. Zhang et al.[38] mentioned that the size of the ceria nanocrystals with 6 nm diameter is so small that the crystal distortion (larger lattice constant) and oxygen vacancies appear. Therefore, we can infer that the short range order structure exist in the amorphous

Table 3
Permeability and porosity of the porous 304 stainless steel substrate.

Sintering temperature and holding time	Porous substrate of stainless steel		
	Porosity (%)	Permeability (Darcy)	Thickness (mm)
1000 °C/1 h	40.4	2.02	1.9
1000 °C/2 h	46.2	1.95	1.9
1000 °C/3 h	46.8	2.12	1.9

phase can be considered as the nanocrystal. That is amorphous phase with oxygen vacancies and serves as the path of oxygen ion conduction. This inference is consistent with the data in Table 2, the as-sprayed anode with lower crystallinity showed higher concentration of oxygen vacancies. After reduction treatment, the crystallinity of the reduced anode is increased and that results in the decreasing of oxygen vacancies. The remainder oxygen vacancies are existed in the reduced anode coating. Use of undoped ceria as an anode material appears to be feasible, so that can reduce production costs in industry. However, the result mentioned above is contradictory to the behavior of the 100% crystalline ceria, that is, oxygen vacancies of the doped ceria are increased in the reduction environment. In fact these two things could not be confused due to the different sources of oxygen vacancy. It needs more evidences to verify our statements. The research work in regard to the oxygen vacancies exist in amorphous undoped ceria is under way; another report will focus on this topic.

3.5. Conductivity of anode coating

Conductivity of the N1 anode coating after reduction by hydrogen was analyzed. Porosity of the anode was up to 34.1%. The conductivity measured by the four-line method (two probes) is shown in Fig. 13. In the room temperature, the anode conductivity was as high as 5000 S/cm. As temperature increased, atomic vibration in the coating increased, as well as moving distance of electrons, the conductivity decreased. At temperature between 500 and 700 °C the conductivity remained between 300 and 200 S/cm. At temperature of 800 °C, the conductivity could be keep in 181.8 S/cm, which consistent with the objective that the anode conductivity at 700 °C should be 200 S/cm. However, compared with other literature, the conductivity with 200 S/cm is improvable. Kwon et al.[39] reported their values are 620 and 190 S/cm at 800 °C for Ni/YSZ coating prepared from various feedstocks materials. All the phases with small size in

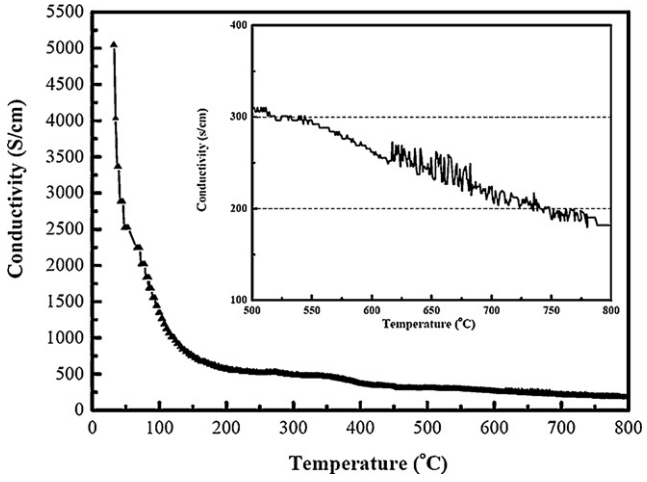

Fig. 13. Relationship between the conductivity and temperature of the reduced N1 anode.

anode have close contact with each other that will lead to more triple phase boundaries and higher conductivity. In our case, however, the NiO particle is comparatively large and the contacts between phases are poor. This is the reason for the inferior electrical conductively of the anode coating.

3.6. Metal support anode

In the third generation of SOFC, thin cermet anode is deposited on metal support to lower the cost. The metal supported solid oxide fuel cells (SOFC) are publicly recognized as a promising alternative to traditional cermet or ceramic supported solid oxide fuel cells. The metal supported solid oxide fuel cells have high mechanical strength, good ductility, and fewer issues in matching thermal expansion coefficients with other devices. As a porous metal support, the porous substrate itself must have good ventilation effect so that fuel can flow smoothly and water, the byproduct of battery reaction, can flow out. Therefore in preparation of porous substrates the porosity and permeability should be intensively explored; high permeability is sustained under certain strength.

As shown in Table 3, the porosity of 304 stainless steel (304SS) did not change significantly, maintained above 40% and the permeability could reach 1.95–2.02 (Darcy). The permeability of the 304SS porous substrate was close to the one of commercial porous substrates. Fig. 14(a) shows surface morphology of the porous 304SS substrate sintering at 1000 °C for 1 h. From the microstructures, the connectivity of pores can be observed. Table 4 shows porosity and permeability of porous

Table 4
Permeability and porosity of the porous nickel substrate.

Sintering temperature and holding time	Porous substrate of nickel		
	Porosity (%)	Permeability (Darcy)	Thickness (mm)
1000 °C/1 h without pore former	32.4	0.03	1.8
1000 °C/2 h without pore former	21.3	0.01	1.8
1000 °C/1 h with spherical PMMA	52.7	0.04	1.8
1000 °C/1 h with elliptic PMMA	54.1	0.15	1.8

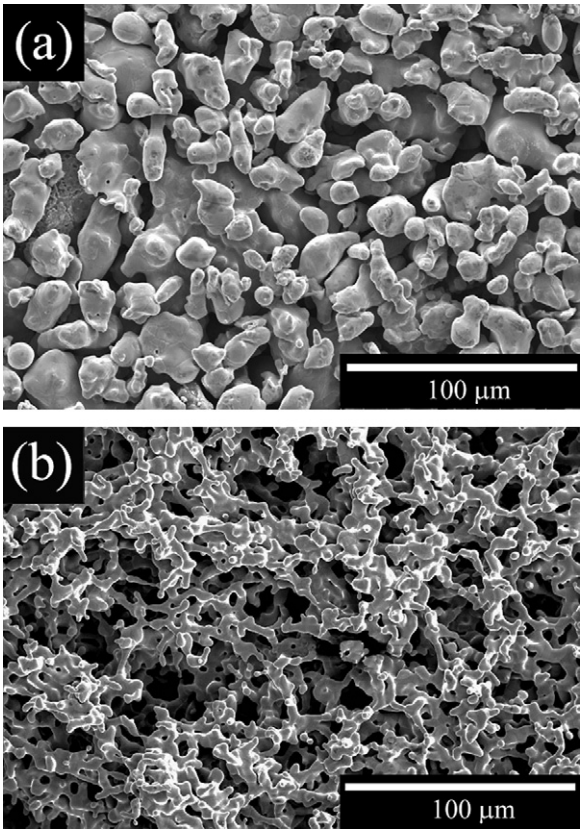

Fig. 14. Morphologies of the porous 304 stainless steel substrate (a), and the porous Ni substrate (b).

nickel substrate sintering at 1000 °C for 1 h and 2 h. The porosity of the nickel substrate apparently decreased with increase of temperature holding time, from 32.4% decreased to 21.3%. Permeability of the nickel substrate was also obviously much lowered, compared with that of porous 304SS substrate. For increasing permeability of the porous nickel substrate, round and oval-shaped PMMA pore formers were added into nickel substrate to enhance connectivity of pores and porosity of the substrate. Table 4 shows that with addition of the PMMA pore former the porosity apparently increased to 52.7% and 54.1%. For permeability, addition of the elliptic PMMA pore former enhanced connectivity of pores in the substrate. The permeability could reach 0.15 (Darcy) higher than that one with spherical PMMA (0.04 Darcy). However, it was some distance to the permeability of commercial porous substrate. Fig. 14(b) shows microstructure of porous nickel substrate sintering at 1000 °C for 1 h. Relative to the 304SS, the porous nickel substrate had more delicate pore structure. Observed from Fig. 14(b), the connectivity of pores was inferior to that in the porous 304SS.

This study tried to use plasma spraying technique on the prepared porous substrates to form anode coatings. Results are shown in Fig. 15, it is found that after coating was sprayed over the porous substrate the surface of the coating contained concave holes of about 50 μm. Large concave holes were easily formed in the coating due to porous property of the porous substrate. In the future, surface planarization or sealing treatment for the pores should proceed before plasma spray in the preparation of the coating.

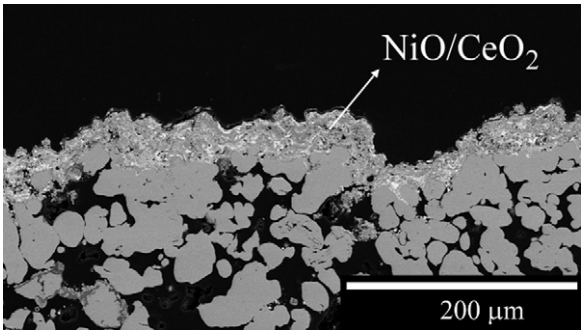

Fig. 15. Cross sectional view of the N1 as-sprayed coating on the porous substrate.

4. Conclusions

Plasma sprayed Ni/CeO_2 anode displayed the well porous microstructure and mechanical property. The N2 coating made from the low spraying power showed the higher porosity than that of the N1 coating made by the high spraying power. The porosity can be up to 37.2% after reduction. On the contrary, the bonding strength of the N1 coating was 33.6 ± 4.8 MPa prepared by high-power spraying, while that was 25.6 ± 3.7 MPa after reduction. The bonding strength of N1 coating is higher than the N2 coating due to the less porosity because of the well melting and impact. It is worth noting that the porosity of the two as-sprayed coatings was more than 30% and the bonding strength is above 24.4 MPa after coating reduction. Both met the specification of general purpose in requirement of whether porosity or bonding strength of coating. In addition, the coating made via high spraying power shows the large amount of amorphous phase and the low crystallinity due to the well melting of feedstocks. From Raman analysis, the amounts of oxygen vacancies in N1 and N2 coating are 0.61 and 0.17 in respectively. The difference of the amount of oxygen vacancy is due to the various crystallinity of the coating. After anode reduction, the oxygen vacancies of ceria in the coatings were decreased. With regard to the electric property, the conductivity of N1 anode could be kept in 181.8 S/cm at 800 °C, consistent with the objective that the anode conductivity at 700 °C should be 200 S/cm. This study tried to use plasma spraying technique on the prepared porous substrates to form anode coatings. It shows that large concave holes were easily formed in the coating during spraying. In the future, surface planarization or sealing treatment for the pores should proceed before plasma spray in the preparation of the coating.

Acknowledgements

The authors acknowledge the financial support from the National Science Council in Taiwan under Contrast Nos. NSC 97-2221-E-027 -080 and NSC 96-2221-E-027-073. We also like to thank the instruments and manpower support by the Materi-

als & Electro-Optics Research Division, Chung-Shan Institute of Science & Technology, Taiwan.

References

1. Zhu WZ, Deevi SC. A review on the status of anode materials for solid oxide fuel cells. *Mater Sci Eng A* 2003;**362**(1–2):228–39.
2. Badwal SPS, Ciacchi FT, Milosevic D. Scandia–zirconia electrolytes for intermediate temperature solid oxide fuel cell operation. *Solid State Ionics* 2000;**136-137**:91–9.
3. Mai A, Haanappel VAC, Uhlenbruck S, Tietz F, Stöver D. Ferrite-based perovskites as cathode materials for anode-supported solid oxide fuel cells. Part I: variation of composition. *Solid State Ionics* 2005;**176**(15–16):1341–50.
4. Nquyen TL, Kobayashi K, Honda T, Iimura Y, Kato K, Neghisi A, Nozaki K, Tappero F, Sasaki K, Shirahama H, Ota K, Dokiya M, Kato T. Preparation and evaluation of doped ceria interlayer on supported stabilized zirconia electrolyte SOFCs by wet ceramic processes. *Solid State Ionics* 2004;**174**:163–74.
5. Holesinger TG, Foltyn SR, Arendt PN, Quanxi J, Dowden PC, DePaula RF, Groves JR. A comparison of buffer layer architectures on continuously processed YBCO coated conductors based on the IBAD YSZ process. *IEEE Trans Appl Supercond* 2001;**11**(1):3359–64.
6. Morgensen M, Skaarup S. Kinetic and geometric aspects of solid oxide fuel cell electrodes. *Solid State Ionics* 1996;**86–88**:1151–60.
7. Meng G, Song H, Dong Q, Peng D. Application of novel aerosol-assisted chemical vapor deposition techniques for SOFC thin films. *Soild State Ionics* 2004;**175**:29–34.
8. Liu Y, Liu M. Porous electrodes for low-temperature solid oxide fuel cells fabricated by a combustion spray process. *J Am Ceram Soc* 2004;**87**:2139–42.
9. Will J, Mitterdorfer A, Kleinlogel C, Perednis D, Gauckler LJ. Fabrication of thin electrolytes for second-generation solid oxide fuel cells. *Solid State Ionics* 2000;**131**:79–96.
10. Pederson LR, Singh P, Zhou XD. Application of vacuum deposition methods to solid oxide fuel cells. *Vacuum* 2006;**80**:1066–83.
11. Young JL, Etsell TH. Polarized electrochemical vapor deposition for cermet anodes in solid oxide fuel cells. *Solid State Ionics* 2000;**135**:457–62.
12. Zha S, Zhang Y, Liu M. Functionally graded cathodes fabricated by sol–gel/slurry coating for honeycomb SOFCs. *Solid State Ionics* 2005;**176**:25–31.
13. Van herle J, Ihringer R, Cavieres RV, Constantin L, Bucheli O. Anode supported solid oxide fuel cells with screen-printed cathodes. *J Eur Ceram Soc* 2001;**21**:1855–9.
14. Monterrubio-Badillo C, Ageorges H, Chartier T, Coudert JF, Fauchais P. Preparation of $LaMnO_3$ perovskite thin films by suspension plasma spraying for SOFC cathodes. *Surf Coat Technol* 2006;**200**:3743–56.
15. Hwang C, Tzeng C. A nanostructured YSZ film coating by liquid suspension injection into an APS plasma flame. *J Adv Oxid Technol* 2005;**8**:85–9.
16. Zhang X, Ohara S, Okawa H, Maric R, Fukui T. Interactions of a $La_{0.9}Sr_{0.1}Ga_{0.8}Mg_{0.2}O_{3-\delta}$ electrolyte with Fe_2O_3, Co_2O_3 and NiO anode materials. *Solid State Ionics* 2001;**139**:145–52.
17. Hui R, Wang Z, Kesler O, Rose L, Jankovic J, Yick S, Maric R, Ghosh D. Thermal plasma spraying for SOFCs: applications, potential advantages, and challenges. *J Power Sources* 2007;**170**:308–23.
18. Takenoiri S, Kadokawa N, Koseki K. Development of metallic substrate supported planar solid oxide fuel cells fabricated by atmospheric plasma spraying. *J Thermal Spray Technol* 2000;**9**(3):360–3.
19. Kesler O. Plasma spray processing of solid oxide fuel cells. *Mater Sci Forum* 2007;**539–543**:1385–90.
20. Zheng R, Zhou XM, Wang SR, Wen TL, Ding CX. A study of Ni + 8YSZ/8YSZ/$La_{0.6}Sr_{0.4}CoO_{3-\delta}$ ITSOFC fabricated by atmospheric plasma spraying. *J Power Sources* 2005;**140**:217–25.
21. Hwang C, Tsai CH, Lo CH, Sun CH. Plasma sprayed metal supported YSZ/Ni–LSGM–LSCF ITSOFC with nanostructured anode. *J Power Sources* 2008;**180**:132–42.
22. Ma X, Dai J, Zhang H, Roth J, Xiao TD, Reisner DE. Solid oxide fuel cell development by using novel plasma spray techniques. *J Fuel Cell Sci Technol* 2005;**2**(3):190–6.
23. Selcuk A, Atkinson A. Elastic properties of ceramic oxides used in solid oxide fuel cells (SOFC). *J Eur Ceram Soc* 1997;**17**:1523–32.
24. Wang BC, Chang E, Lee TM, Yang CY. Changes in phases and crystallinity of plasma-sprayed hydroxyapatite coatings under heat treatment: a quantitative study. *J Biomed Mater Res* 1995;**29**:1483–92.
25. Zyman Z, Cao Y, Zhang X. Periodic crystallization effect in the surface layers of coatings during plasma spraying of hydroxyapatite. *Biomaterials* 1993;**14**:1140–4.
26. A STM C 633-79. Standard test method for adhesion or cohesive strength of flame-sprayed coatings.
27. Yashima M, Arashi H, Kakihana M, Yoshimura M. Raman scattering study of cubic-tetragonal phase transition in $Zr_{1-x}Ce_xO_2$ solid solution. *J Am Ceram Soc* 1994;**77**:1067–71.
28. McBride JR, Hass KC, Poindexter BD, Weber WH. Raman and X-ray studies of $Ce_{1-x}RE_xO_{2-y}$, where RE = La, Pr, Nd, Eu, Gd, and Tb. *J Appl Phys* 1994;**76**:2435–41.
29. Lin XM, Li LP, Li GS, Su WH. Transport property and Raman spectra of nanocrystalline solid solutions $Ce_{0.8}Nd_{0.2}O_{2-\delta}$ with different particle size. *Mater Chem Phys* 2001;**69**:236–40.
30. Dohčević-Mitrović ZD, Šćepanović MJ, Grujić-Brojčin MU, Popović ZV, Bošković SB, Matović BM, Zinkevich MV, Aldinger F. The size and strain effects on the Raman spectra of $Ce_{1-x}Nd_xO_{2-\delta}$ ($0 \le x \le 0.25$) nanopowders. *Solid State Commun* 2006;**137**:387–90.
31. Spanier JE, Robinson RD, Zhang F, Chan SW, Herman IP. Size-dependent properties of CeO_{2-y} nanoparticles as studied by Raman scattering. *Phys Rev B* 2001;**64**:245407.
32. Kostic R, Askrabic S, Dohcevic-mitrovic Z, Popovic ZV. Low-frequency Raman scattering from CeO_2 nanoparticles. *Appl Phys A* 2008;**90**:679–83.
33. Anwar MS, Kumar S, Ahmed F, Arshi N, Seo YJ, Lee CG, Koo BH. Study of nanocrystalline ceria thin films deposited by e-beam technique. *Curr Appl Phys* 2010, doi:10.1016/j.cap.2010.11.053.
34. Liang C, Ma Z, Lin H, Ding L, Qiu J, Frandsen W, Su D. Template preparation of nanoscale $Ce_xFe_{1-x}O_2$ solid solutions and their catalytic properties for ethanol steam reforming. *J Mater Chem* 2009;**19**:1417–24.
35. Mineshige A, Taji T, Muroi Y, Kobune M, Fujii S, Nishi N, Inaba M, Ogumi Z. Oxygen chemical potential variation in ceria-based solid oxide fuel cells determined by Raman spectroscopy. *Solid State Ionics* 2000;**135**:481–5.
36. Reddy BM, Thrimurthulu G, Katta L, Yamada Y, Park SE. Structural characteristics and catalytic activity of nanocrystalline ceria-praseodymia solid solutions. *J Phys Chem C* 2009;**113**:15882–90.
37. Pu ZY, Lu JQ, Luo MF, Xie YL. Study of oxygen vacancies in $Ce_{0.9}Pr_{0.1}O_{2-\delta}$ solid solution by in situ X-ray diffraction and in situ Raman spectroscopy. *J Phys Chem C* 2007;**111**:18695–702.
38. Zhang G, Shen Z, Liu M, Guo C, Sun P, Yuan Z, Li B, Ding D, Chen T. Synthesis and characterization of mesoporous ceria with hierarchical nanoarchitecture controlled by amino acids. *J Phys Chem B* 2006;**110**:25782–90.
39. Kwon O, Kumar S, Park S, Lee C. Comparison of solid oxide fuel cell anode coatings prepared from different feedstock powders by atmospheric plasma spray method. *J Power Sources* 2007;**171**:441–7.